Friction

Research Article

Mutual promotion on the mechanical and tribological properties of the nacre-like self-lubricant film designed for demanding green tribological applications

Hongbo Ju[1,2,3,†,✉], Jing Luan[2,†], Yiping Wang[1], Andrey Bondarev[4], Manuel Evaristo[2], Yaoxiang Geng[1], Junhua Xu[1], Albano Cavaleiro[2], Filipe Fernandes[2,5]

Cite this article: Ju HB, Luan J, Wang YP, et al. *Friction* 2025, **13**(3): 9440963. https://doi.org/10.26599/FRICT.2025.9440963

ABSTRACT: The inverse relationship between the tribological and mechanical properties of environmentally friendly self-lubricant films, induced by the addition of soft lubricant agents that can diffuse quickly at elevated temperatures, has hindered the widespread use of these materials in industrial applications. This paper took this challenge to break through the above established relationship by developing novel nacre-like multilayered Mo_2N–SiN_x/Ag–SiN_x self-lubricant films via an radio frequency (RF) magnetron sputtering system for real applications where harsh conditions at elevated temperatures exist. The multilayered films, deposited by alternating deposition of Mo_2N–SiN_x and Ag–SiN_x modulation layers, exhibited three phases of face-centered cubic (fcc) Mo_2N, fcc Ag and SiN_x, where SiN_x encapsulated the nano-crystalline Mo_2N and Ag phases in each layer to successfully induce a "brick and mortar" nacre-like microstructure (in the area without the coherent structure). The epitaxy growth of the Ag–SiN_x layers with thickness below 6 nm on the Mo_2N template resulted in an extraordinary increase in both the hardness and elastic modulus, which was able to prevent severe degradation of the mechanical properties caused by the addition of Ag. The room-temperature anti-friction property could be enhanced by increasing the Ag–SiN_x layer thickness due to the excellent lubricant nature of Ag, which acts in synergy with Mo_2N, while the wear rate below 4×10^{-8} mm³/(N·mm) was due to the high mechanical strength. The tribological properties at 600 °C also benefited from the interlocked multilayered architecture, which allowed an extreme low friction coefficient of ~0.12 and a negligible wear rate (WR). This behavior was attributed to the synergism between the lubricant action of Ag and Mo_2N and the tribo-phase transformation from $Ag_2Mo_4O_{13}$ to Ag_2MoO_4.

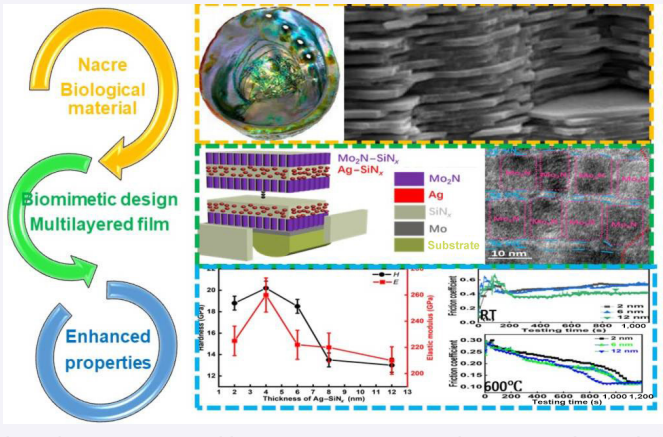

KEYWORDS: radio frequency (RF) magnetron sputtering system; Mo_2N–SiN_x/Ag–SiN_x self-lubricant films; interlocked structure; epitaxial growth; lubrication synergism; tribo-phase transformation

1 Introduction

Friction and wear are inevitable factors contributing to energy consumption in every industry sector [1]. The development of versatile and environmentally friendly lubricants, with the aim of substituting fossil fuel derivatives, has consistently been seen as the most direct path to fulfilling the demands of a more environmentally sustainable future and achieving energy conservation goals [2–4]. Friction and wear are predominantly surface-related phenomena. Therefore, modifying the surfaces through the deposition of low-friction films provides a means to address the limitations of liquid lubricants, such as restricted operational temperature ranges, limited load-bearing capacity, highly costly recycling processes, and their unsuitability for use in

† Hongbo Ju and Jing Luan contributed equally to this work.

[1] School of Materials Science and Engineering, Jiangsu University of Science and Technology, Zhenjiang 212003, China. [2] Department of Mechanical Engineering, ARISE, CEMMPRE, University of Coimbra, Coimbra 3030-788, Portugal. [3] TINT - Laboratory for Tribology and Interface Nanotechnology, Faculty of Mechanical Engineering, University of Ljubljana, Aškerčeva 6, Ljubljana, 1000, Slovenia. [4] School of Engineering, Bernal Institute, University of Limerick, Limerick V94 T9PX, Ireland. [5] ISEP-School of Engineering , Polytechnic of Porto, Porto 4200-072, Portugal.

✉ Corresponding author. E-mail: hbju@just.edu.cn, hju@uc.pt

Received: April 3, 2024; Revised: June 22, 2024; Accepted: July 3, 2024

vacuum environments and corrosive media [5]. Over the last decade, potential chemically inert solid lubricant agents with low shear moduli (e.g., Ag and Au) have been widely introduced into hard ceramic-based films to achieve enhanced tribological performance over a wide temperature range [6–12]. Although improved tribological performance can often be attained in composite films by incorporating appropriate amounts of potential lubricant agents, the rapid diffusion of these agents toward the film's surface can lead to premature component failure when exposed to elevated temperatures [13–15]. Furthermore, lubricant agents are often soft phases that can degrade the overall mechanical strength of composite films [16, 17]. However, through advanced film design, it is possible to accelerate the implementation of these films in various industrial applications. Another critical challenge when self-lubricating films are applied in industrial settings is the necessity to simultaneously improve their long-term lubrication capabilities across a wide temperature range while simultaneously maintaining their mechanical properties.

Two main effective approaches have been reported for achieving long-term self-lubrication through controlling the release of lubricant agents: (i) One is the composite configuration, which involves adding a protection phase into the self-lubricant matrix to protect the lubricant agents from oxidation and diffusion to the surface. For example, WC and WS_2 nano-size particles were added to an amorphous diamond-like carbon (DLC) matrix prepared by physical vapor deposition (PVD), and the results confirmed the efficient protection of the DLC to achieve long-term lubrication under humidity testing conditions [18–20]. Amorphous SiN_x (a-SiN_x) was also introduced into self-lubricant nitride-based films, such as Mo_2N–Cu [21], Mo_2N [22], and TiN–Ag [23], to synthesize a composite film in which a low release of lubricant agents was reported. (ii) A multilayered architecture containing barrier layers [24, 25] whose tribological properties were improved by inserting SiN_x layers into the main Mo_2N–Ag film [26]. This enhancement can be attributed to the gradual release of Ag at elevated temperatures [26]. Nevertheless, the obvious interface between adjacent layers easily induces interlayer delamination under the shear force arising during sliding. Moreover, the difference in chemical/physical compatibility degrades the cohesion of the films.

On the other hand, it seems extremely difficult to achieve the goal of simultaneously maintaining excellent self-lubrication with a high level of mechanical strength. In fact, excellent self-lubricant properties require a suitable content of a soft potential lubricant agent. For example, more than 15 at% soft metal (SMe) is mandatory for achieving satisfactory elevated-temperature lubricant properties of transition metal nitride (TMN)–SMe films [27]. Magnetron-sputtered TiN–Ag composite films were reported to exhibit the best lubricating performance from room temperature (RT) up to 500 °C when the Ag/(Ag+2Ti) ratio was 45 at%, which leads, in this case, to a hardness of only 8 GPa [28]. Ag and Cu were added into Ti-Al-N hard films deposited by PVD, and the results confirmed that 20 at% of Ag and Cu enhanced the anti-frictional properties, resulting in a friction coefficient (CoF) of ~0.1 at the cost of decreasing the hardness down to ~7 GPa [29]. Similar results have also been reported in other systems of TaN–Ag [30], VN–Ag [31, 32], and NbN–Ag [33] films.

Achieving a balance between long-term lubrication and mechanical properties of self-lubricating films remains a challenge in the field of solid lubrication nowadays. It is essential to prevent both excessive diffusion of lubricant agents to the surface and the reduction of the overall mechanical properties due to the addition of soft components.

The design and fabrication of biomimetic materials inspired from nature has been widely reported as an efficient method to remarkably enhance their properties [34] because of the amazing well-organized biological microstructure resulting from millions of years of evolution [35]. One of the striking examples of these materials is the mother-of-pearl, also known as nacre [36]. Its fully evolved microstructure of ceramic tablets densely packed and bonded together by a thin layer of biopolymer [36], resulted in mechanical properties, including elastic modulus, yield strength and toughness, much better than those of each individual layer of nacre [37]. Some biomimetic materials were designed on the basis of the unique microstructure of nacre, with a "brick and mortar" characteristic [38]. In this study, a novel interlocked structure design inspired by the "brick and mortar" microstructure of nacre is applied to develop Mo_2N–SiN_x/Ag–SiN_x multilayered self-lubricant films. This approach enables the development of environmentally friendly solid lubricants by simultaneously enhancing both their lubricating and mechanical properties: (i) The nacre-like structure, by introducing SiN_x to encapsulate the lubricant agent of either Mo_2N or Ag, will protect Mo_2N against oxidation and Ag from anti-diffusion, respectively, at elevated temperatures; (ii) the suitable content of the lubricant agents of Mo_2N and Ag can be easily deposited into the separated modulation layered structure to maintain excellent self-lubricant properties at a wide range of temperatures; (iii) the thickness of Mo_2N–SiN_x and Ag–SiN_x layers will be changed to induce coherency between the phases to compensate for the influence of the low mechanical strength of Ag. Therefore, Mo_2N–SiN_x/Ag–SiN_x multilayered films were deposited using radio frequency (RF) magnetron sputtering with the thickness of Mo_2N–SiN_x fixed at 15 nm and the thickness of Ag–SiN_x varying from 2 to 12 nm. Then, the influence of the interlocked structure of the film on the mechanical and tribological properties is discussed.

2 Experimental

2.1 Deposition process

A series of Mo_2N–SiN_x/Ag–SiN_x multilayered films were prepared using high-purity (99.9%) Mo, Si, and Ag targets (Deyang ONA new materials Co., Ltd., China) by RF magnetron sputtering (Fig. 1). Polished high-speed steel W18Cr4V (W18) and Si(100) wafers (Deyang ONA new materials Co., Ltd., China) were used as substrates, and their roughnesses were approximately 0.4 and 50 nm, respectively. Before deposition, the substrates were ultrasonically cleaned in alcohol for 15 min and then in acetone for 15 min. High-speed steel substrates were used for tribo-tests at room and elevated temperatures, whilst Si substrates were used for microstructural studies and measurements of mechanical properties. The distance between the targets and substrates was set to 80 mm. Before deposition, the chamber was pumped down below 6.0×10^{-4} Pa. First, a Mo adhesion layer with a thickness of ~150 nm was deposited with an Ar flow rate of 10 standard cubic centimeters per minute (sccm) to improve the adhesion between the film and the substrate. Following this, the multi-layer structure was created by alternately opening the shutters for the Mo and Ag targets while keeping the Si target shutter open. In all deposition processes, the films were produced by applying power levels of 250, 80, and 80 W to the Mo, Si, and Ag targets, respectively, under a deposition pressure of 0.3 Pa and a gas mixture of Ar/N_2 at a ratio of 10/3. By adjusting the opening time of the shutter on the sputtering Mo and Ag targets, various multilayered films were

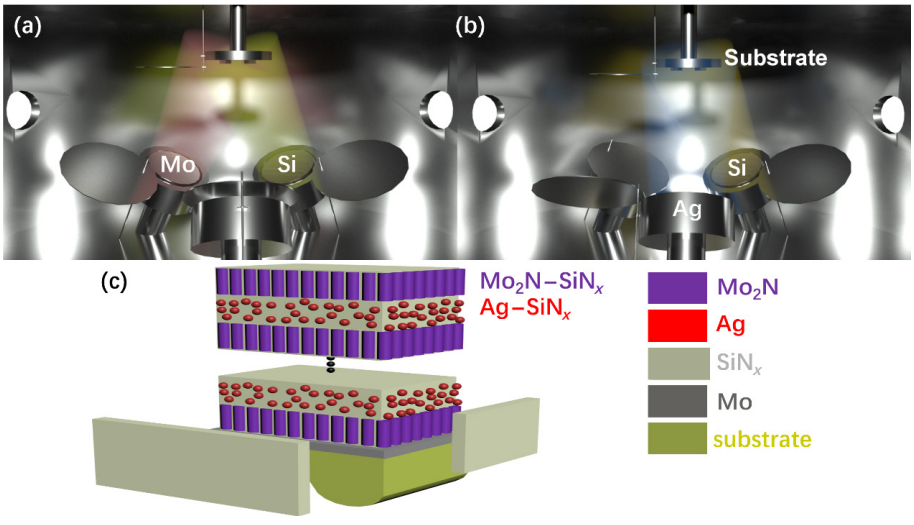

Fig. 1 3D schematic image of the deposition of multilayered films: (a) deposition of $Mo_2N–SiN_x$ layers, (b) deposition of $Ag–SiN_x$ layers, and (c) 3D schematic image of multilayered film.

produced. These films maintained a consistent $Mo_2N–SiN_x$ layer thickness of 15 nm, while the $Ag–SiN_x$ layer thickness was varied from 2 to 12 nm. No bias or substrate heating was applied during the deposition. The total thickness designed for all the multilayered films was approximately 2.0 μm.

2.2 Structural characterization

The crystal structure of $Mo_2N–SiN_x/Ag–SiN_x$ films was determined by an X-ray diffractometer (XRD; Shimazu-6000, Shimazu, Japan) with Cu Kα radiation at a passing energy of 160 eV and 2θ in the range of 20°–80° with a step of 0.4°. The samples for TEM analysis were prepared using an FEI Helios G4CX dual-beam system (Thermo Fisher Scientific, USA) with a Ga^+ ion source after a protective W mask was deposited. The acceleration voltage for focused ion beam (FIB) milling was 30 kV for rough operations, followed by 5 and 2 kV for final polishing. The FIB lamellae were examined via an FEI Titan Themis^3 S/transmission electron microscopy (TEM) microscope (Thermo Fisher Scientific, USA) operating at 300 kV. Using an energy-dispersive X-ray (EDS) Super-XG1 detection system with 4 windowless silicon drift detectors (SDDs), elemental mapping of the samples was performed.

2.3 Mechanical and tribological characterizations

The hardness (H) and elastic modulus (E) were measured by a nano-indenter (CPX+NHT2+MST, Anton Paar, Switzerland), with a constant loading force of 3 mN and holding time of 10 s. To ensure the accuracy of the results, 15 measurements were conducted in 2 different zones of the samples. The RT and 600 °C wear tests were conducted in a pin-on-disc tester (UMT-2, CETR, USA) using alumina balls (diameter of 9.4 mm) as counterparts in open air. The rotation speed was 50 r/min, and the sliding time was 20 min; the applied load was 3 N, and the radius of the wear track was 4 mm. During RT wear tests, the relative humidity was ~30%. After the wear tests, the average friction coefficient of the films was taken from the steady-state zone of their corresponding friction curves. The two-dimensional (2D) profiles of the wear tracks were measured using a three-dimensional (3D) profiler (Dektak-XT, Bruker, Germany), and the wear rates (WRs) of the films were obtained using Archard's law. SEM observations and a Raman spectrometer (inVia, Renishaw, UK), were used to study wear tracks.

3 Results and discussion

3.1 Micro(structure)

Figure 2 shows the XRD patterns of the reference monolayered $Mo_2N–SiN_x$ and $Ag–SiN_x$ films and multilayered $Mo_2N–SiN_x/Ag–SiN_x$ films. The diffraction pattern of the $Mo_2N–SiN_x$ monolayer film reveals a fcc structure, assigned to fcc-Mo_2N (JCPDF No. 15-2366) phase with the corresponding (111), (200), (220), (311), and (222) diffraction peaks. Moreover, another diffraction peak at 2θ of ~69° was detected from the Si substrate. Probably, a dual phase of fcc-Mo_2N and amorphous SiN_x can co-exist in the $Mo_2N–SiN_x$ monolayer film, in a capsule-like structural characteristic with the Mo_2N grains encapsulated by an amorphous SiN_x phase, as presented in previous papers [21, 39]. In the case of $Ag–SiN_x$ monolayer film, no obvious diffraction peaks can be observed except for those from the Si substrate due to the relatively low intensity of the Ag diffraction peaks (the diffraction peaks of Ag were observed in our previous paper [12]). Based on our previous high-resolution TEM (HRTEM) results [12], this monolayer film can exhibit a dual phase of fcc-Ag nanoparticles embedded in an amorphous SiN_x matrix. Therefore, the Ag metallic phase present in the form of small clusters can explain the absence of XRD peaks. The XRD patterns of all multilayered films, regardless of the thickness of the $Ag–SiN_x$ layer, exhibit two different series of diffraction peaks, which are assigned to the fcc-Mo_2N and Si substrates. The diffraction peaks are located at lower angles than those from the monolayered $Mo_2N–SiN_x$ film. This shift is related to the epitaxial deposition of $Ag–SiN_x$ layers on the Mo_2N template (see the HRTEM section): The epitaxy structure easily induces compressive stresses in the Mo_2N phase due to the lower lattice parameter of Ag in relation to that of Mo_2N, resulting in a dilatation in the perpendicular directions and, thereby, the diffraction peaks of Mo_2N shifting to lower angles. However, the compressive stress could be released by further increasing the number of $Ag–SiN_x$ layers above 6 nm, since epitaxy should not be possible throughout the entire $Ag–SiN_x$ layer.

The state of the chemical bonds in the monolayered films has been discussed in our previously published works [26, 39, 40], and the results are in good agreement with the evolution of the XRD patterns presented in Fig. 2. The dual-phases of both fcc-Mo_2N and amorphous SiN_x co-exist in the $Mo_2N–SiN_x$ monolayer film since both the Mo–N bonds [21, 41] (fcc-Mo_2N) and Si–N bonds

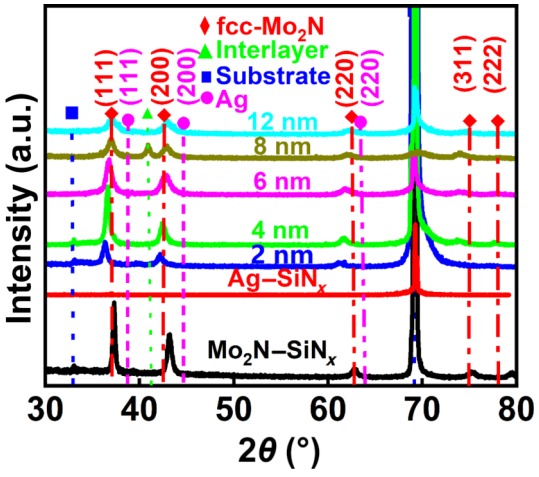

Fig. 2 XRD diffraction patterns of reference Mo_2N–SiN_x and Ag–SiN_x monolayer films, and Mo_2N–SiN_x/Ag–SiN_x multilayered films with varied thickness of Ag–SiN_x layers.

[42–44] (amorphous SiN_x) can be detected in the X-ray photoelectron spectroscopy (XPS) spectrum. The Ag–Ag bonds [12], referred to as the nanoparticles of Ag, and the Si–N bonds [12] in amorphous SiN_x appear in the XPS spectrum of the Ag–SiN_x monolayer film. This also confirms the presence of embedded Ag nanoparticles in the amorphous matrix.

To obtain detailed information about the structure of the multilayer films and their interfacial characteristics, TEM was used, as shown in Fig. 3. The cross-sectional high-angle annular dark-field (HAADF) image of a multilayer film is shown in Fig. 3(a), and an obvious contrast between Mo_2N–SiN_x and Ag–SiN_x layers can be seen. The bright and dark layers in this figure correspond to Mo_2N–SiN_x and Ag–SiN_x, respectively. The thickness of each layer aligns well with the intended design: approximately 15 nm for Mo_2N–SiN_x and 4 nm for Ag–SiN_x. The selected area electron diffraction (SAED) image acquired from the multilayered specimen in Fig. 3(a) is shown in Fig. 3(b), with the ring patterns corresponding to the (111), (200), (220), and (311) reflections characteristics of the fcc phase. In accordance with the XRD analysis shown in Fig. 2, a significant contribution to the electron diffraction patterns of the Ag phase is not expected; moreover it can be hard to separate these signals due to the very close lattice parameters of Mo_2N and Ag. The high-resolution HAADF image and its corresponding Ag and Mo EDS element maps are shown in Figs. 3(c) and 3(d). The Ag in the Ag–SiN_x layer is not distributed homogeneously and forms only clusters with a diameter of ~4 nm. This suggests that the Ag particles are embedded into the SiN_x matrix. These results are similar to those reported for the Ag–SiN_x monolayer system deposited with different silver contents [12].

HRTEM was used to further investigate the cross-sectional microstructure characteristics of the film with 4 nm SiN_x layer, and the results are shown in Fig. 4. Figure 4(a) shows an obvious multilayered architecture consisting of bright Ag–SiN_x and dark Mo_2N–SiN_x layers. The amorphous and crystal phases co-exist in the Mo_2N–SiN_x layer, and the crystal phase refers to fcc-Mo_2N based on its lattice fringe with a spacing of 0.246 nm (fcc-Mo_2N(111), JCPDF No. 15-2366). The coherency characteristics could be detected in the right half of this figure, with obvious lattice fringes throughout several layers of Ag–SiN_x and Mo_2N–SiN_x. Either Ag or SiN_x in the Ag–SiN_x layers contributes to the epitaxy structure, since the discontinuous Ag nanoparticles are too small (Fig. 3(d)) to fully contribute to the epitaxy area in Fig. 4(a). The Ag–SiN_x layers without coherency with the Mo_2N template were observed to be in a mixed crystalline and amorphous state (Fig. 4(a)). The corresponding monolayer film also exhibits a dual phase of fcc-Ag and amorphous SiN_x based on our previous results [12]. Each modulation layer, either Ag–SiN_x or Mo_2N–SiN_x, consists of amorphous and crystalline phases, where the Mo_2N or Ag crystallites are surrounded by an amorphous tissue in the region without the coherency characteristic. Moreover, it is hard to observe the interface characteristics in the amorphous region of the Mo_2N–SiN_x layer with the Ag–SiN_x one. High density of stacking faults (SFs) are also detected in each layer, the region marked with a yellow line. The fast Fourier transforms (FFTs) in Figs. 4(c)–4(e), all with the [011] zone axis (z.a.), derived from the center of Mo_2N–SiN_x (area A), Mo_2N–SiN_x+Ag–SiN_x (area B), and Mo_2N–SiN_x layers (area C), exhibit only one set of spots corresponding to the fcc phase. This result also confirms the existence of coherent interface regions between layers and the epitaxial growth of fcc-Ag on the fcc-Mo_2N template. Figure 4(f) shows the HRTEM bright field (BF) image of the multilayered film from the interface region, which is aligned along the [011] zone axis. The dual interface

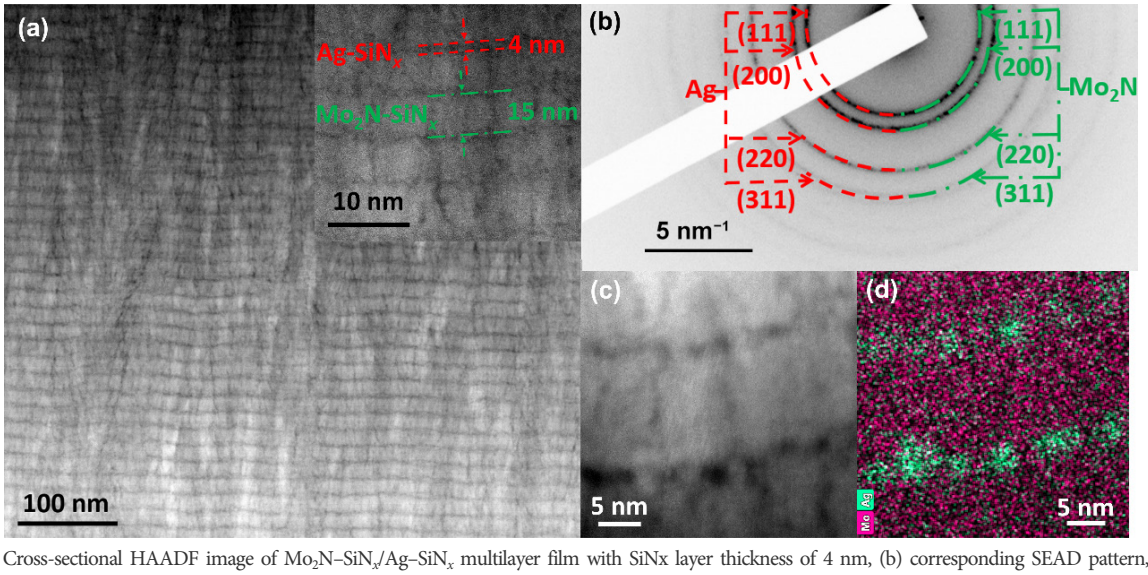

Fig. 3 (a) Cross-sectional HAADF image of Mo_2N–SiN_x/Ag–SiN_x multilayer film with SiNx layer thickness of 4 nm, (b) corresponding SEAD pattern, (c) high-magnification HAADF image, and (d) its corresponding Ag and Mo elements mapping.

characteristics, including both completely coherent and semi-coherent characteristics, could be detected, and obvious dislocations appear in the semi-coherent regions.

The TEM results of the cross-sectional multilayer film with a SiN_x layer thickness of 6 nm are shown in Fig. 5. Figure 5(a) shows the HAADF dark-field (DF) image of the film where the

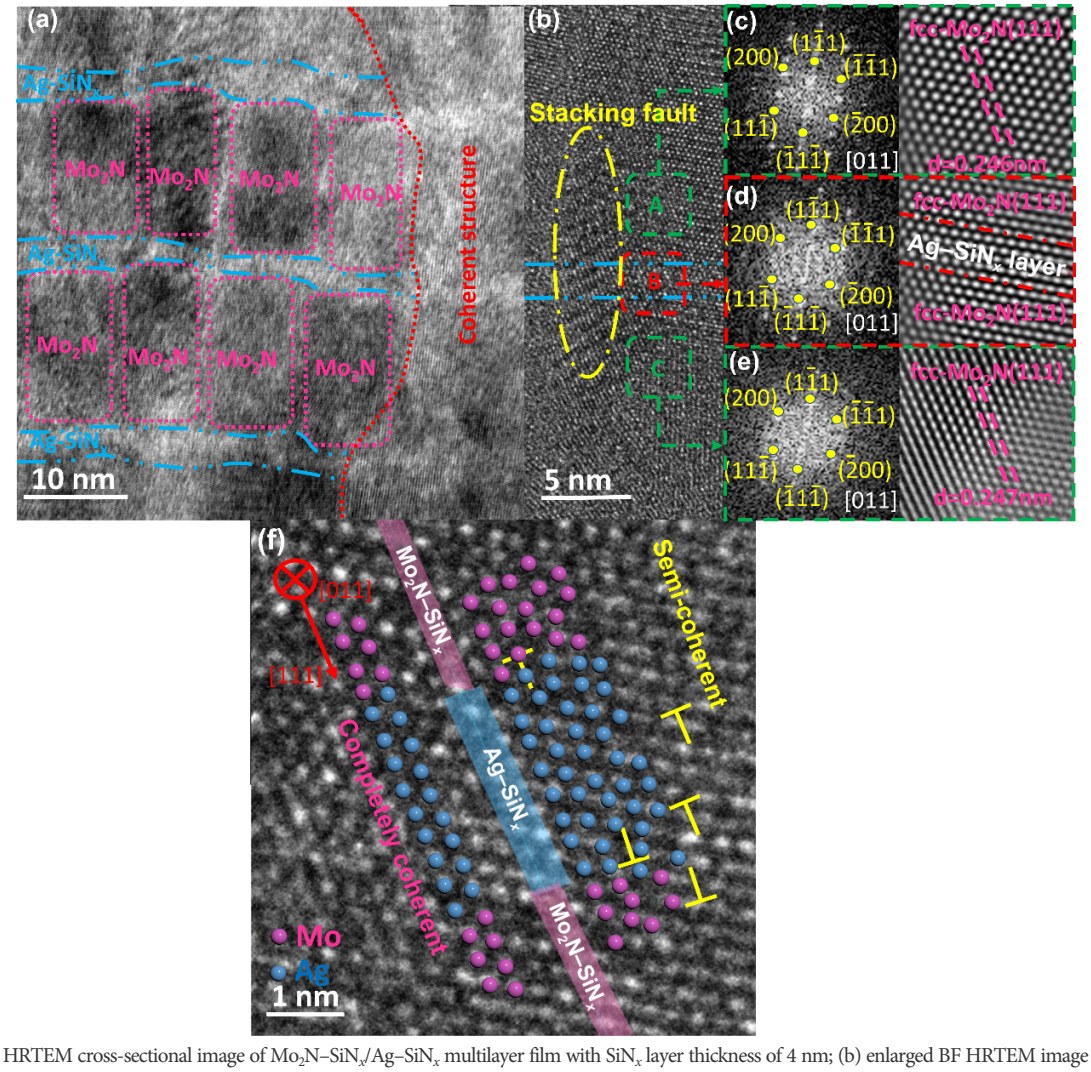

Fig. 4 (a) BF HRTEM cross-sectional image of Mo_2N–SiN_x/Ag–SiN_x multilayer film with SiN_x layer thickness of 4 nm; (b) enlarged BF HRTEM image of film and its corresponding FFT pattern in areas of (c) A, (d) B, and (e) C in (b); (f) BF HRTEM image from interface area of film.

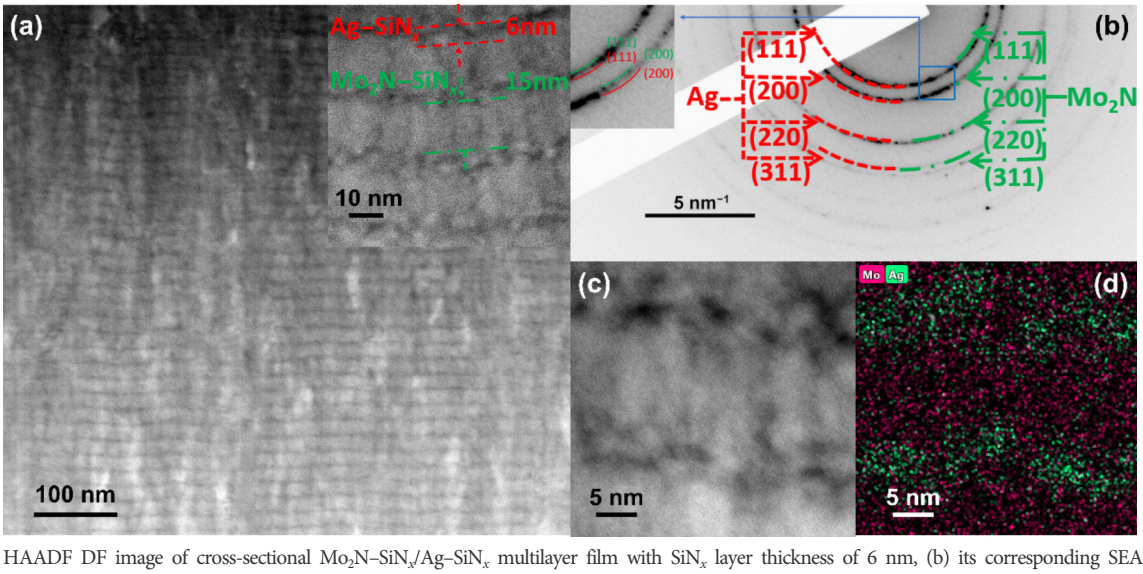

Fig. 5 (a) HAADF DF image of cross-sectional Mo_2N–SiN_x/Ag–SiN_x multilayer film with SiN_x layer thickness of 6 nm, (b) its corresponding SEAD pattern, (c) enlarged HAADF DF image, and (d) its corresponding Ag and Mo elements mapping.

interface between adjacent layers is still detected. The thickness of the Mo_2N–SiN_x layer in the film is ~15 nm, but the thickness of the SiN_x layer increases to ~6 nm (inset of Fig. 5(a)). Discontinuous white particles (Ag due to its high atomic number) can be detected in the inset of Fig. 5(a). Only one set of diffraction rings appear in Fig. 5(b), corresponding to the (111), (200), (220), and (311) reflections characteristic of the fcc phase. The enlarged HAADF DF cross-sectional image of the multilayer film (Fig. 5(c)) further confirms the presence of discontinuous Ag particles in the Ag–SiN_x layer, which is related to the poor wettability of metal Ag on the surface of the ceramic-based template, either Mo_2N or SiN_x, and its low solubility in the SiN_x matrix [12]. The corresponding Ag and Mo element mapping data are shown in Fig. 5(d). The results confirm the multilayered architecture of the film with Ag nanoparticles of the diameter in the range of 2–5 nm.

HRTEM BF images for the cross-section of the multilayered film at the 6 nm SiN_x layer are depicted in Fig. 6 to further investigate the phase structure and interface characteristics. The light region in Fig. 6(a) refers to SiN_x, whereas the grey and dark regions correspond to Mo_2N and Ag, respectively, due to their different atomic numbers. Nanoparticles of Ag are uniformly distributed in the Ag–SiN_x layers, and the characteristic nanocapsule arrangement of the crystalline Mo_2N grains encapsulated by amorphous SiN_x could be detected in the Mo_2N–SiN_x layers in the region without the coherency characteristic. An interlocked structure is then also formed, similar to a multilayered film with a 4 nm Ag–SiN_x layer (Fig. 4). A higher-magnification HRTEM image, shown in Fig. 6(b), also confirms that the average diameter of the Ag nanoparticles is in the range of 2–5 nm inside the Ag–SiN_x layers. The average width of the crystalline Mo_2N grains and the thickness of the encapsulated amorphous SiN_x in the Mo_2N–SiN_x layers are ~10 and ~3 nm, respectively. The FFT pattern from region A in Fig. 6(b) is shown in Fig. 6(c), and two series of spots referring to an fcc structure can be detected. However, its corresponding inverse fast fourier transform (IFFT) image, as shown in Fig. 6(d), exhibits the same lattice arrangement with a plane spacing of ~0.247 nm, which is close to that of fcc-Mo_2N(111) (JCPDF No. 15-2366). Thus, the coherency structure still exists in the multilayer film but cannot cross throughout several modulation layers, such as the one with an Ag–SiN_x layer of 4 nm.

The interfaces of the multilayered films significantly depend on the critical thickness of the Ag–SiN_x layers, based on the above HRTEM results, and two possibilities of forming the coherency structure between the Mo_2N–SiN_x layer and its adjacent Ag–SiN_x layers: (i) The fcc-Ag particles epitaxially grow from the fcc-Mo_2N template, and (ii) the SiN_x layer grows epitaxially and forms coherent interfaces with the template. The width of the coherency area is larger than the size of Ag nanoparticles in the Ag–SiN_x layers, based on the results shown in Fig. 4, and consequently, both Ag and SiN_x contribute to the formation of the coherency structure. The critical thickness of each phase epitaxy with the template can be evaluated as follows.

As for the coherency structure between SiN_x and Mo_2N, the re-crystallization of SiN_x layer with a thickness of several nanometers, resulting from nitride-based templates such as TiN [45, 46], AlN [47], and ZrN [48, 49], could be accomplished via the multilayered architecture to decrease the total Gibbs free energy. Therefore, the total energy (E_T) per unit area of fcc-SiN_x ($E_T^{w-Si_3N_4}$) should be lower than that of a-SiN_x ($E_T^{a-Si_3N_4}$) : $E_T^{w-Si_3N_4} < E_T^{a-Si_3N_4}$. If the SiN_x layer epitaxially grows with the Mo_2N template to form fcc-SiN_x, the $E_T^{w-Si_3N_4}$ and $E_T^{a-Si_3N_4}$ can be calculated based on Eqs. (1) and (2):

$$E_T^{w-Si_3N_4} = 2E_I^{w-Si_3N_4/c-AlN} + E_b^{w-Si_3N_4}t + E_s t \tag{1}$$

$$E_T^{a-Si_3N_4} = 2E_I^{a-Si_3N_4/c-AlN} + E_b^{a-Si_3N_4}t \tag{2}$$

where E_I, E_b, E_s, and t are the interface energy, volumetric energy, strain energy, and thickness of the SiN_x layer, respectively.

The critical thickness (t_c) of the SiN_x layer epitaxially growing with the template fcc-Mo_2N could be calculated based on Eqs. (3) and (4):

$$t_c = \frac{2(E_I^{a-Si_3N_4/c-AlN} - E_I^{w-Si_3N_4/c-AlN})}{E_b^{w-Si_3N_4} - E_b^{a-Si_3N_4} + \frac{1}{2}Y\epsilon^2} \tag{3}$$

$$E_s = \frac{1}{2}Y\varepsilon^2 \tag{4}$$

where Y and ε are the modulus and strain in the interlayer of SiN_x, respectively.

The above equations can be derived as follows, since the interface energy is very low because the coherency structure reduces the number of interfaces.

$$t_c = \frac{4E_I^{a-Si_3N_4/fcc-Mo_2N}}{Y\epsilon^2} \tag{5}$$

$$\varepsilon_A = \frac{f}{1+\frac{G_A t_A}{G_B t_B}} \tag{6}$$

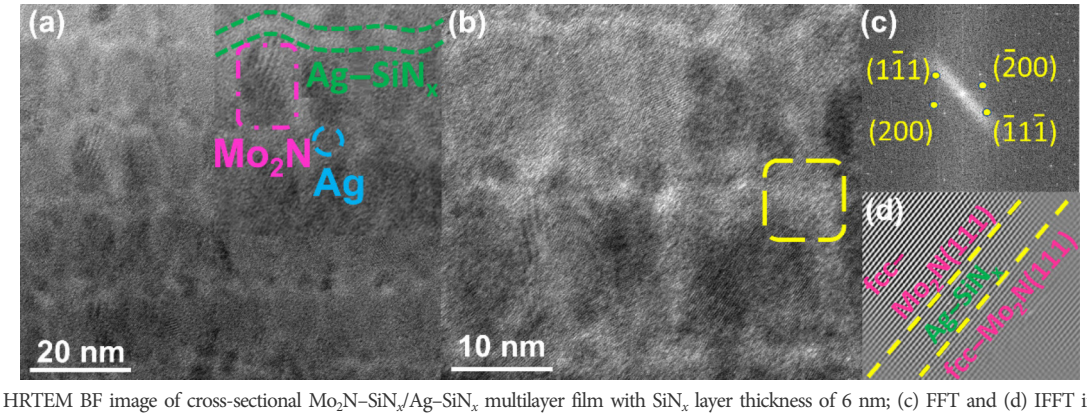

Fig. 6 (a, b) HRTEM BF image of cross-sectional Mo_2N–SiN_x/Ag–SiN_x multilayer film with SiN_x layer thickness of 6 nm; (c) FFT and (d) IFFT image from the coherency region (region A).

$$f = \frac{a_f - a_s}{a_s} \quad (7)$$

where G is the shear modulus; t is the thickness of the film; subscript A represents Mo_2N–SiN_x layer; subscript B represents Ag–SiN_x layer; f is the mismatch of the modulation layers; a_f is the lattice constant of fcc-Mo_2N; a_s is the lattice constant of the one epitaxial growth with fcc-Mo_2N.

The critical thickness of SiN_x epitaxially grown with the Mo_2N template is 0.9 nm based on the above equations. This calculated value is in good agreement with the experimental result from the SiN_x/Mo_2N multilayer film exhibiting a coherency structure with a SiN_x layer thickness of 0.8 nm [22]. However, the multilayer film in this study for the < 6 nm Ag–SiN_x layer still has a coherent structure; thus, fcc-Ag could be considered the main factor because of the low lattice mismatch between Ag(111) and Mo_2N(111). The critical size of Ag nanoparticles epitaxially growing with the nitride-based template was also proved around 4 nm in our previous Ref. [27].

Based on above results, the Mo_2N–SiN_x/Ag–SiN_x multilayer film formed by alternating deposition of Mo_2N–SiN_x and Ag–SiN_x layers exhibits three phases of fcc-Mo_2N, fcc-Ag, and SiN_x (SiN_x exhibits an amorphous state in the region without a coherency structure but could be crystalline in the coherency zone), regardless of the Ag–SiN_x layer thickness. This nano-interlocked structure characteristic of multilayer films is formed by (i) the embedding of Ag nanoparticles into the SiN_x matrix in the Ag–SiN_x layer and (ii) the encapsulation of Mo_2N by a SiN_x shell in the Mo_2N–SiN_x layer. The coherency structure could be detected in the multilayer film at the ≤ 6 nm Ag–SiN_x layer, and the largest region of the coherency structure, crossing several modulation layers, could still be detected for the multilayer film at the 6 nm Ag–SiN_x layer.

3.2 Mechanical and tribological properties

The hardness and elastic modulus of the multilayer films as a function of the Ag–SiN_x layer thickness, as well as the corresponding monolayer films of Mo_2N–SiN_x and Ag–SiN_x, are shown in Fig. 7. The hardness and elastic modulus calculated based on rule-of-mixture (ROM) are also shown in Fig. 7 as a reference to confirm the extraordinary increase in both the hardness and elastic modulus induced by the nano-multilayered architecture. The measured hardness values of the Mo_2N–SiN_x and Ag–SiN_x monolayer films are ~17.2 and ~7.5 GPa, respectively. The ROM hardness of the multilayer film decreases gradually with the increase of Ag–SiN_x layer thickness. However, the multilayered architecture by alternating the Mo_2N–SiN_x (15 nm) and Ag–SiN_x (≤ 6 nm) nano-sized layerscould enhance the hardness, and its tested value increases from ~18.5 GPa for the film with the Ag–SiN_x layer thickness of 2 nm to ~20.6 GPa for the film of the Ag–SiN_x layer thickness of 4 nm. The hardness of the multilayered film decreases gradually from ~18.3 GPa for the film with the 6 nm Ag–SiN_x layer to ~14.3 GPa for the film with the 8 nm Ag–SiN_x layer, which is very close to the ROM. With a further increase in thickness, the hardness value slightly decreases, which is in good agreement with the ROM value. The coherent interface could not cross from one to the other Mo_2N–SiN_x layers, although it still exists in some areas of the Ag–SiN_x layer with the adjacent Mo_2N template. This coherency is lost inside the Ag–SiN_x layer because of the high Ag–SiN_x layer thickness (≥ 8 nm) and, consequently, relaxing the lattice to less distortion, as well as less hardness, approaching the one from ROM.

The special mechanical characteristic of super-hardness, with an extreme hardness value of above 70 GPa or higher than that of diamond, which occurs for a modulation period of less than 10 nm by a nano-multilayered/composite architecture, has been reported for many novel nano-sized materials [50]. The multiple phases in the Mo_2N–SiN_x/Ag–SiN_x multilayer film result in a remarkable increase in hardness due to the influence of multiple factors, such as the following.

(i) The coherency strain: The completely or semi-coherent interface of the multilayered film with the Ag–SiN_x layer thickness below 6 nm (based on the TEM results) could not fully release the coherency stresses in the film and, hereby, inhibit the partial dislocation motion based on the coherent strain principle, ultimately increasing the hardness of the multilayered films [51].

(ii) Different values of the elastic modulus of each modulation layer. The dislocation energy per unit length of each layer significantly depends on its shear modulus and, consequently, avoids dislocations moving across the interface between the modulation layers to maintain a state of low energy [52]. Thus, it induces a mirror-like stress, referred to as an alternating stress field, such that an additional shear stress with a value at least above G/100 (G is the shear modulus of the layer with a lower modulus) is needed for the dislocation to overcome [53].

(iii) The region of high-density SFs existing in the multilayered film at the 4 nm Ag–SiN_x layer also results in a hardness enhancement since the movement of the dislocations across the interface could be inhibited by the SFs [54, 55]. A classic equation was reported to estimate the resistance capacity (τ) of the SF to the partial dislocation as Eq. (8) [56]:

$$\tau = \frac{\mu b^2 (2+\nu)}{8\pi (1-\nu) w} \quad (8)$$

where μ is the shear modulus; b is the Burgers vector; ν is the

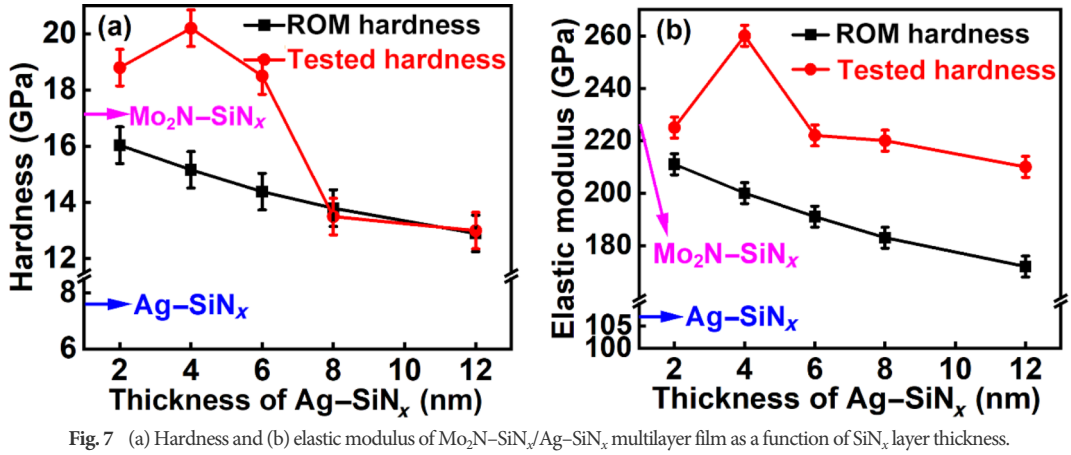

Fig. 7 (a) Hardness and (b) elastic modulus of Mo_2N–SiN_x/Ag–SiN_x multilayer film as a function of SiN_x layer thickness.

清華大学出版社 Tsinghua University Press | SciOpen

Poisson's ratio; w is the SF width. Therefore, the value of τ calculated using the data in Fig. 4 is ~1.5 GPa, thereby contributing to the hardness enhancement.

The elastic moduli of the monolithic Mo_2N–SiN_x and Ag–SiN_x films are ~225 and ~108 GPa, respectively, as depicted in Fig. 7(b), and the ROM of the multilayered film gradually decreases with the increase of the Ag–SiN_x layer thickness. However, the elastic moduli of all the multilayer films tested, regardless of the Ag–SiN_x layer thickness, are greater than the ROM. Moreover, it initially increases and then decreases with the increase of the Ag–SiN_x layer thickness after reaching a maximum value of ~260 GPa at the 4 nm Ag–SiN_x layer.

The remarkable increase in the elastic modulus for the multilayer films in relation to the expected values predicted by a mixture law can be explained by the existence of coherency from both Ag and SiN_x phases. An increase in the crystallinity is, then, expected with the consequent increase in the elastic modulus. For the 4 nm Ag–SiN_x layer, the coherency through the Ag–SiN_x layer is maximized, which results in the peak value shown in Fig. 7(b).

Figure 8 shows representative friction curves and average friction coefficients (CoFs) at RT. A running-in stage, regardless of the thickness of SiN_x layer, could be detected in the friction curves. At the beginning of the test, in the running-in, the friction coefficient gradually increases, reaching a local maximum value, and then decreases until it reaches a stable value. The duration of the running-in stage is extended as the Ag–SiN_x layer thickness increases in the multilayer film. At the beginning of the wear test, the contact between the two sliding surfaces is done through the asperities of the film and ball, which are removed under the shear force; then, the debris will form the initial transfer layer on the contact area. The excess debris will accumulate either in the front of the sliding ball or on both sides of the wear track. Some hard debris could be further incrusted on the surface of the film, resulting in the rise of the friction coefficient at this time. The Ag–SiN_x layer, where epitaxial growth is reduced, exhibits low hardness and, consequently, is easily removed under the shear force to form the transfer layer, resulting in an increase in the maximum frictional force in the running-in stage. Therefore, the maximum friction coefficient in the running-in stage increases gradually with the increase of the Ag–SiN_x layer thickness. The decrease in the friction coefficient after the running-in stage might be attributed to the formation of a lubricant transfer layer including the lubricant tribo-phases as well as the lubricant debris of Ag and Mo_2N. For all the films, after the running-in stage, the friction coefficient is stable throughout the rest of the test.

The average CoF values of the multilayered films, shown in Fig. 8(b), first remain stable close to ~0.50 for the 2–6 nm Ag–SiN_x layer films and then decrease gradually from ~0.45 to ~0.41 for the 12 nm Ag–SiN_x layer film.

Figure 9 shows the wear track morphologies of the multilayer films after the wear test at RT. All the coated samples are not completely worn out, since the maximum depth of the wear track, regardless of the Ag–SiN_x layer thickness, is less than 2 μm. The obvious scratches on the wear track surface of all the multilayered films in Fig. 9 also confirm the effect of the asperities on the formation of hard particles that are transferred to the third body formed during the running-in stage of the friction curves, as shown in Fig. 8(a). Moreover, similar detailed information of the wear track for each sample from four different regions, including the depth, width, and accumulation of the transfer layers, can be observed in Fig. 9, indicating a continuous stable contact of the counterpart with the sample during the wear test. Figures 9(a) and 9(b) show a narrow wear track depth after the tribotest of the multilayer film at the 2 nm Ag–SiN_x layer, with depths and widths of ~1.1 and ~300 μm, respectively. The accumulation of worn-out material appears on both (A and C regions) or single (B and D regions) sides of the wear track, with a darker color. The tribo-chemical actions with the counterpart and the sample induce the formation of tribo-phases during the slide, and consequently, the tribolayers accumulate on the side of the wear track. A wider wear track with a width of ~500 μm is detected as the Ag–SiN_x layer thickness increases to 6 nm (Figs. 9(c) and 9(d)); however, the depth remains at a similar value of ~1.1 μm. The slight decrease in hardness corresponds to a low load-bearing capacity of the film and consequently increases the contact area with the counterpart under the same load. The increase in the Ag–SiN_x layer thickness also enlarges the dark region areas on either the center (Fig. 9(a)) or the sides (Figs. 9(b)–9(d)) of the wear track, where the transfer layers accumulate on the surface, as shown in Fig. 9(c). The number of scratches on the wear track surface also increases compared with that observed in Fig. 9(a). The brittle but hard SiN_x-based debris from the Ag–SiN_x layer moving along with its counterpart during the wear test might be responsible for this. Increasing the Ag–SiN_x layer thickness to 12 nm further enlarges the dark area, covering almost the entire surface of the wear track, as shown in Fig. 9(e). Although deep scratches could be detected on the track surface, the number of scratches obviously decreased. A decrease in the hardness of a sample slightly increases the width of the wear track to ~550 μm. However, a shallower wear track depth appears during this period, with a maximum value of ~1.0 μm, which could result from the adhesion of transfer layers. This also leads to the lowest value of the wear rate for all multilayered samples.

Figure 10 depicts the influence of the Ag–SiN_x layer thickness

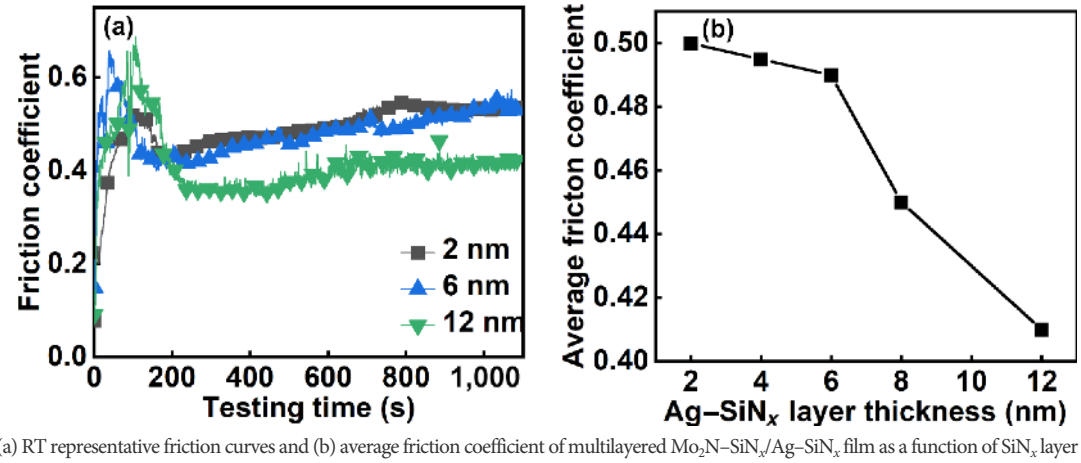

Fig. 8 (a) RT representative friction curves and (b) average friction coefficient of multilayered Mo_2N–SiN_x/Ag–SiN_x film as a function of SiN_x layer thickness.

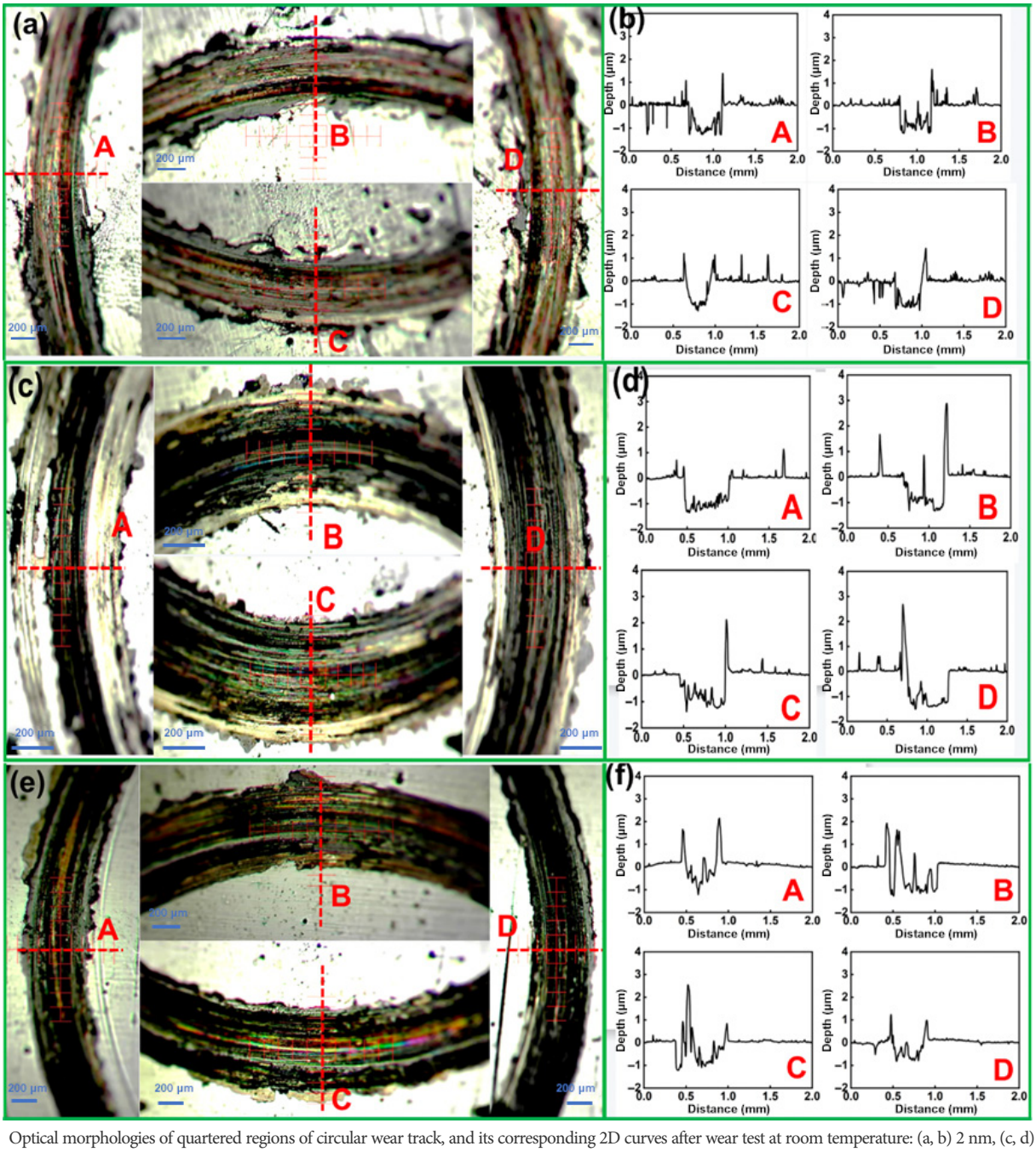

Fig. 9 Optical morphologies of quartered regions of circular wear track, and its corresponding 2D curves after wear test at room temperature: (a, b) 2 nm, (c, d) 6 nm, and (e, f) 12 nm.

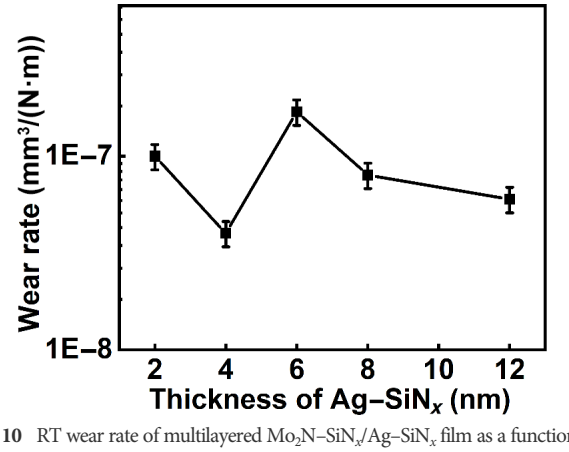

Fig. 10 RT wear rate of multilayered Mo_2N–SiN_x/Ag–SiN_x film as a function of SiN_x layer thickness

on the RT WR against the counterpart of Al_2O_3. The WR of the multilayer film at the 2 nm Ag–SiN_x layer is ~1.0×10^{-7} mm³/(N·mm) and drops significantly to ~4.1×10^{-8} mm³/(N·mm) when the Ag–SiN_x layer increases to 4 nm but increases again to ~1.7×10^{-7} mm³/(N·mm) for the film at the 6 nm Ag–SiN_x layer. Then, the WR gradually decreases with a further increase of the Ag–SiN_x layer thickness from 8 to 12 nm. The lowest value of WR is registered for the film at the 4 nm Ag–SiN_x layer, which has the highest hardness, and the film at the 12 nm Ag–SiN_x layer has the second lowest value of WR; however, in this case, the factor that contributes to this result is the highest amount of soft phase that results in a lower friction.

Figure 11 shows the Raman spectra after the RT wear tests as well as the Raman spectrum from outside of the wear track of the film at the 2 nm Ag–SiN_x layer, corresponding to the as-deposited film. The as-deposited film exhibits no obvious Raman peaks that

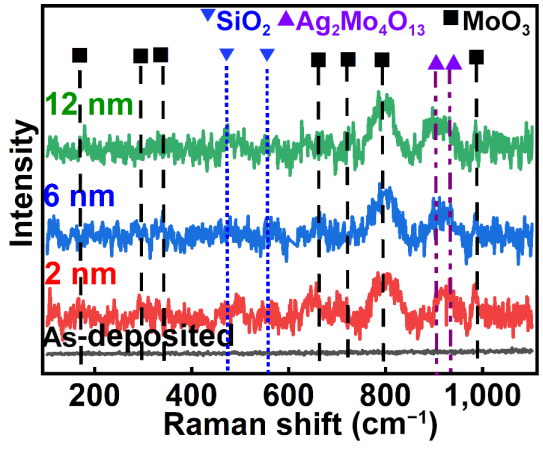

Fig. 11 Raman spectra from as-deposited and wear track of Mo_2N–SiN_x/Ag–SiN_x multilayer film after wear test at RT.

could be associated with the formation of any compound. However, on the wear track for all the films, the Raman peaks corresponding to $Ag_2Mo_4O_{13}$ and MoO_3 can be identified in all the spectra. This finding indicates that the transfer layer on the wear track surface might have similar tribo-phase components for all of the tested films. Double layers of distorted edge-sharing MoO_6 octahedra parallel to the (010) planes are in the MoO_3 phase, with only van der Waals forces holding the successive layers. Therefore, a low shear strength occurs during the wear test [57]. Layered MoO_3 has been widely reported as a classic self-lubricant tribo-phase, which is easily formed on the sliding surfaces by complex tribo-chemical actions during wear tests either at RT or elevated temperatures, enhancing the anti-frictional performance [39, 58]. The appearance of $Ag_2Mo_4O_{13}$ tribo-phase, rather than Ag_2MoO_4 or $Ag_2Mo_2O_7$, could be expected given the high mole percentage of Mo in the films, based on the MoO_3-Ag/Ag_2O phase diagram. Wenda [59] reported an interesting experimental result of easy formation of $Ag_2Mo_4O_{13}$ at RT without any heating through the investigation on the powder mixture of MoO_3 and Ag or Ag_2O, which was maintained for a long period of time. Thus, it is reasonable to form the tribo-phase of $Ag_2Mo_4O_{13}$ tribo-chemical processes at RT wear tests after the induction of MoO_3 tribo-phase formation, according to Reaction (9) [59]:

$$2Ag + 4MoO_3 + 1/2O_2 \rightarrow Ag_2Mo_4O_{13} \quad (9)$$

or (10):

$$2Ag + 4MoO_3 + H_2O \rightarrow Ag_2Mo_4O_{13} + H_2 \quad (10)$$

The double metal oxide tribo-phase also exhibits excellent self-lubricant characteristics during the wear test [60]. Moreover, vestiges of Raman peaks at ~460 and ~520 cm^{-1}, corresponding to SiO_2 [61], could be detected. The hard phase of SiO_2 phase in the transfer layer is responsible for the appearance of scratches on the wear track surface.

Based on the above, the tribological properties of the multilayer films at RT are significantly influenced by the Ag–SiN_x layer thickness: The lowest CoF can be obtained for the film with a 12 nm Ag–SiN_x layer, which has satisfactory wear resistance performance; however, the lowest WR is detected for the film with a Ag–SiN_x layer of 4 nm due to its excellent mechanical properties.

Several factors influence the anti-friction characteristics:

(i) Transfer layers. Lubricant tribo-phases, including $Ag_2Mo_4O_{13}$ and MoO_3, co-exist in the transfer layers to lubricate the wear track and consequently drop the CoF.

(ii) Contact area. A large contact area induced by the low hardness of the film with thickness of Ag–SiN_x layer > 6 nm may result in relatively high friction during the wear test. However, the enlarging transfer layer area is also detected for the film with a large contact area, thereby enhancing the anti-friction properties to drop the CoF.

(iii) Ag–SiN_x layer thickness. The Ag–SiN_x monolayer film has a relatively low CoF below 0.40 under the same testing conditions [12] because of the excellent lubricant nature of pure Ag phase, as well as the lubricant synergism between SiN_x and Ag. The thick Ag–SiN_x layers inserted into the Mo_2N–SiN_x matrix enhance the anti-friction properties.

A balance among the contact area, Ag–SiN_x layer thickness, and transfer layer could be achieved, and then, the CoF gradually decreased for the film with the thickness of Ag–SiN_x layer > 6 nm.

For the WR of the film, the influent factors are as follows:

(i) The mechanical properties of the films can significantly influence their wear resistance properties at RT. A higher mechanical strength is similar to a higher load-bearing capacity [62, 63], which ultimately leads to a smaller contact area with the counterpart. In addition, the toughness could be enhanced by the epitaxy architecture [64], improving the wear resistance property. This could be considered a main factor resulting in the low WR for the film with a 4 nm Ag–SiN_x layer.

(ii) Another important issue that could also be taken into consideration to investigate the WR is the anti-friction properties. Although the widest wear track could be detected for the film at the 12 nm Ag–SiN_x layer, owing to its lower hardness, its lowest CoF, softens the contact between the film and its counterpart, and gives rise to a shallower wear track, resulting in a low WR.

Figure 12 illustrates the friction curves of the Mo_2N–SiN_x/Ag–SiN_x multilayer films with 2, 6, and 12 nm Ag–SiN_x layers at 600 °C. The friction coefficient of the film, regardless of the Ag–SiN_x layer thickness, can be divided into three stages: (i) The first stage is the running-in, which occurs at the beginning of the wear test, where the friction coefficient strongly fluctuates, with an increase in the beginning of the test for short time of less than 80 s. (ii) Then, the friction coefficient gradually decreases with time for all the samples. The increase of the Ag–SiN_x layer thickness induces a decrease in the friction coefficient throughout the test in relation to that of the mother films. Moreover, the time to reach the low stable value of the friction coefficient decreases from ~1,000 s for the 2 nm Ag–SiN_x layer down to ~750 s for the 12 nm Ag–SiN_x layer. (iii) In the last stage, the friction coefficient

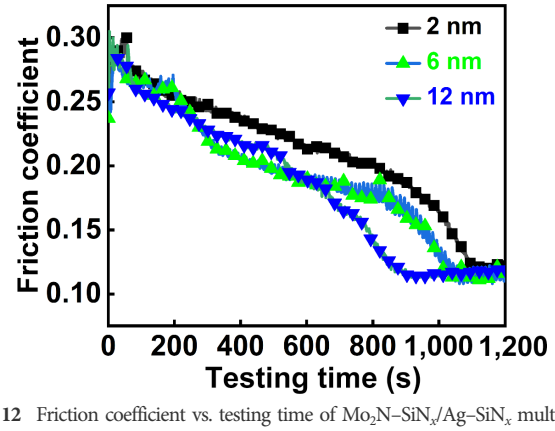

Fig. 12 Friction coefficient vs. testing time of Mo_2N–SiN_x/Ag–SiN_x multilayer film at 600 °C.

of the film is independent of the Ag–SiN_x layer thickness, with a remarkable value of ~0.12 at the end of the test.

The Raman spectra of the wear track surface after the 700 s and 1,200 s wear test durations are shown in Fig. 13 to investigate the evolution of the tribo-phases with the testing time at 600 °C. The Raman peaks attributed to MoO_3 [65] and $Ag_2Mo_4O_{13}$ [66] can be detected in the wear tracks of both samples after 700 s, as shown in Fig. 13(a). However, a new tribo-phase of Ag_2MoO_4 [67] is detected in the Raman spectra of the wear track after 1,200 s, with the disappearance of $Ag_2Mo_4O_{13}$ phase. In addition, the definition and intensity of Ag_2MoO_4 peaks increase with the increase of Ag–SiN_x layer thickness. This suggests that more Ag_2MoO_4 tribo-phases form on the wear track to influence the tribological properties at 600 °C for the multilayer films with thicker Ag–SiN_x layers. The evolution of Ag-based binary transition metal oxide tribo-phases can be understood from the Raman results. The $Ag_2Mo_4O_{13}$ phase can be easily formed after the development of MoO_3 in the wear test at 600 °C by the tribo-chemical action according to Reaction (11) [59]:

$$2Ag + 4MoO_3 + 1/2O_2 \rightarrow Ag_2Mo_4O_{13} \quad (11)$$

or (12):

$$Ag_2O + 4MoO_3 \rightarrow Ag_2Mo_4O_{13} \quad (12)$$

The thickness of the transfer layer, induced by tribochemical and/or physical action under the counterpart, gradually increases with increasing test time at 600 °C, and then, the initially relatively fast diffusion is avoided, resulting in the evolution of $Ag_2Mo_4O_{13}$ into Ag_2MoO_4 [68] via Reactions (13) and (14) [59]:

$$2Ag + Ag_2Mo_4O_{13} \rightarrow 2Ag_2Mo_2O_7 \quad (13)$$

$$Ag + Ag_2Mo_2O_7 + 1/2O_2 \rightarrow 2Ag_2MoO_4 \quad (14)$$

Layered Ag_2MoO_4 has been reported as one of the most common lubricant materials for applications at elevated temperatures [69] because of its weak Ag–O bonds linking [MoO_4] tetrahedra to [AgO_6] octahedra [70]. Therefore, the evolution of the tribo-phase of Ag-based binary transition metal oxide from $Ag_2Mo_4O_{13}$ to Ag_2MoO_4 with the increase of the test time during the wear test at 600 °C could be considered the main factor responsible for the evolution of friction in the second and third stages for multilayer films at 600 °C, as follows.

(i) The lubricant tribo-phases of MoO_3 and $Ag_2Mo_4O_{13}$ can form on the wear track surface, governing lubrication during the wear test, with their contents increasing with continuous contact with their counterparts. This results in a gradual decrease in the friction coefficient with increasing test duration after the running-in stage.

(ii) The evolution of the tribo-phase from $Ag_2Mo_4O_{13}$ to Ag_2MoO_4 also enhances the anti-friction performance, resulting in a decrease in the friction coefficient as a function of testing time.

(iii) The total phase transformation to Ag_2MoO_4 leads to the appearance of the third stage of the curve, with a friction coefficient value of ~0.12.

(iv) The low melting point of Ag_2MoO_4 at ~570 °C could induce solid-liquid lubrication to further enhance the anti-friction properties, thereby contributing to the extremely low coefficient of ~0.12 in the third stage of the friction curve.

Figure 14 illustrates the optical wear track images and their corresponding 2D morphologies of the multilayered films after the wear test at 600 °C. Although the wear tracks of all the films, regardless of the Ag–SiN_x layer thickness, can be detected, their depth is too shallow to calculate the WR. In addition, the roughness of the area outside the wear track increases gradually with the increase of Ag–SiN_x layer thickness. Despite the multilayer configuration, the diffusion of Ag at 600 °C may occur despite the excellent anti-diffusion capacity of amorphous SiN_x, as proven in our previous work on Ag–SiN_x monolayer films [12].

The pretended wear resistance, at 600 °C, is achieved by the interlocked multilayered architecture due to the following reasons:

(i) The excellent anti-friction properties, especially the solid–liquid lubrication induced by the low melting point of Ag_2MoO_4 tribo-phase, could soften the interaction with the counterpart, and hence, the extremely low friction coefficient contributes to the enhancement of the wear resistance.

(ii) The diffusion of Ag in SiN_x matrix during the wear test toward the surface of the film compensates for the wear under the counterpart during the wear test.

(iii) The wear resistance properties could benefit from the volume expansion induced by the evolution of the tribo-phase from $Ag_2Mo_2O_7$ to Ag_2MoO_4 [71].

(iv) The interlocked structure of the multilayered film effectively prevents interlayer delamination under shear forces during sliding contact because of the difference in the physical/chemical characteristics of each layer at elevated temperatures.

4 Conclusions

A series of nacre-like interlocked multilayered films with

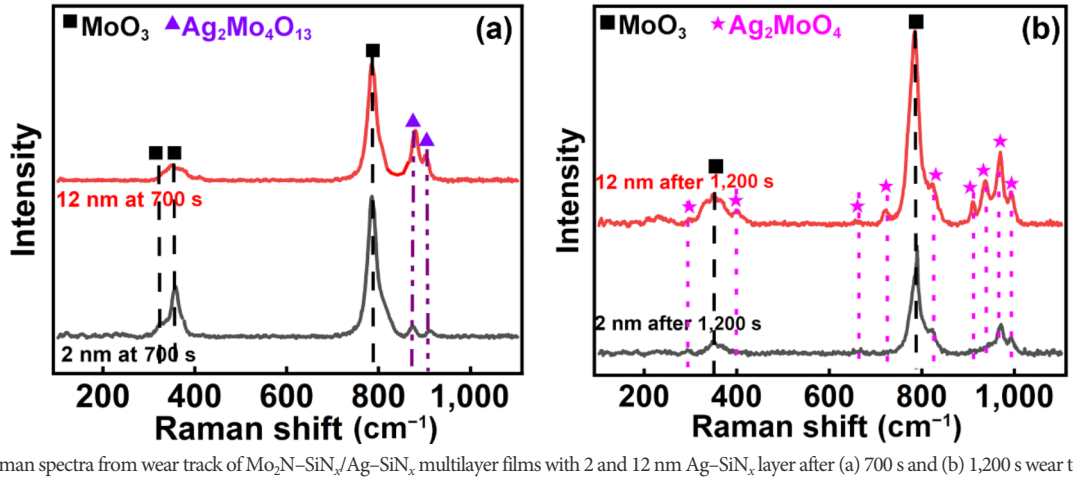

Fig. 13 Raman spectra from wear track of Mo_2N–SiN_x/Ag–SiN_x multilayer films with 2 and 12 nm Ag–SiN_x layer after (a) 700 s and (b) 1,200 s wear test at 600 °C.

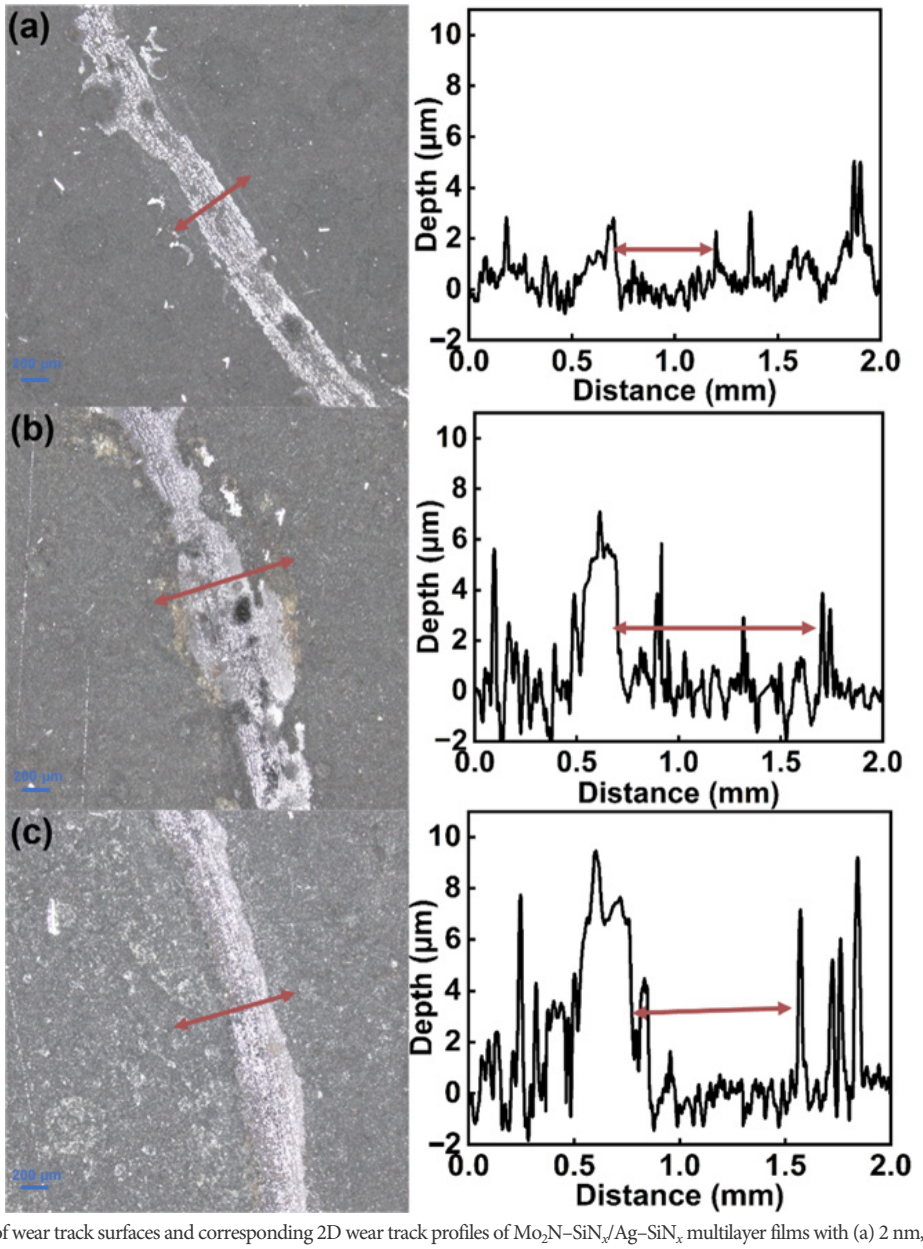

Fig. 14 Optical images of wear track surfaces and corresponding 2D wear track profiles of Mo_2N–SiN_x/Ag–SiN_x multilayer films with (a) 2 nm, (b) 6 nm, and (c) 12 nm Ag–SiN_x layer after wear test at 600 °C.

alternating Mo_2N–SiN_x and Ag–SiN_x nanolayers were designed and deposited using RF magnetron sputtering for a wide range of temperatures in key applications. For this purpose, several requirements need to be met: (i) the adequate formation of lubricant tribo-layers to ensure self-lubricant properties at RT and elevated temperatures by a tribological synergism between Mo_2N and Ag; (ii) the prevention of excessive diffusion of the lubricant agents toward the surface to achieve long-term lubrication by the introduction of a SiN_x phase to form an interlocked structure; (iii) the appropriate blocking of the degradation of the mechanical properties to enhance the wear resistance by the coherent strengthening of the Ag–SiN_x layer below 6 nm. The influence of the Ag–SiN_x nanolayer thickness on the microstructure and mechanical and tribological properties of the multilayered films was investigated, and the main conclusions can be drawn as follows:

(1) In the zone without the coherency characteristic, a dual phase of fcc-Mo_2N and SiN_x co-existed in the Mo_2N–SiN_x layers, with amorphous SiN_x encapsulating Mo_2N nano-crystalline phase; the Ag–SiN_x layers exhibited a dual phase of fcc-Ag and amorphous SiN_x, with the Ag nanoparticles embedded into an amorphous matrix. However, the thickness of the Ag–SiN_x layer below 6 nm could induce the coherency structure in some areas where Ag or Ag–SiN_x could epitaxially grow over the Mo_2N template.

(2) Inserting the Ag–SiN_x layer (≤ 6 nm) into the Mo_2N–SiN_x matrix induced a remarkable increase in hardness, which was attributed mainly to the coherent strengthening induced by the epitaxial growth of the Ag–SiN_x layers over the Mo_2N template layers. The coherency structure also led to an increase in the elastic modulus. Both the hardness and elastic modulus of the multilayered film with > 6 nm Ag–SiN_x layer followed the rule of mixture, with values close to the weighted average of those of the individual layers.

(3) The RT average friction coefficient of the multilayered film decreased gradually from ~0.50 for the 2–6 nm Ag–SiN_x layer to ~0.41 for the 12 nm Ag–SiN_x layer; the anti-friction performance of the Ag–SiN_x layer and the lubricant tribo-phases of $Ag_2Mo_4O_{13}$

and MoO_3 increased the formation of lubricious materials during the wear test. Excellent RT wear resistance was detected for all multilayered films, with wear rates ranging from 4×10^{-8} to 1×10^{-7} mm³/(N·mm). The lowest values of the friction and wear coefficients were found for the films with 4 and 12 nm Ag–SiN_x layers.

(4) At 600 °C, in all multilayer films, the friction coefficient gradually decreased with testing time, reaching a value of ~0.12 at the end of the test. This behavior was attributed to the evolution of the formation of the lubricant tribo-phases. The diffusion of Ag toward the surface, as well as the tribo-phase transformation from $Ag_2Mo_4O_{13}$ to Ag_2MoO_4, contributed to the excellent wear resistance properties, with a very shallow wear track, not allowing to calculate the wear rate.

Acknowledgements

This work was supported by projects granted by the National Natural Science Foundation of China (Nos. 52171071 and 51801081), national funds through FCT of Portugal–Fundação para a Ciência e a Tecnologia, under a scientific contract of 2021.04115. CEECIND, 2023.06224.CEECIND, and the projects of UIDB/00285/2020, and LA/0112/2020, MCTool21-ref. "POCI-01-0247-FEDER-045940" co-financed via FEDER and FCT-Fundação para a Ciência e a Tecnologia (COMPETE). The projects of UIDB/00285/2020, and LA/0112/2020. The Slovenian Research Agency ARIS under the Research Core Funding Programme No. P2-0231 and the project MSCA-COFUND-5100-237/2023-9. This work was also supported by the Outstanding University Young Teachers of "Qing Lan Project" of Jiangsu Province of China and the Excellent Talents of "Shenlan Project" of Jiangsu University of Science of China.

Declaration of competing interest

The authors have no competing interests to declare that are relevant to the content of this article.

References

[1] Woydt M. Material efficiency through wear protection—The contribution of tribology for reducing CO_2 emissions. *Wear* **488–489**: 204134 (2022)
[2] Perry S S, Tysoe W T. Frontiers of fundamental tribological research. *Tribol Lett* **19**(3): 151–161 (2005)
[3] Korkmaz M E, Gupta M K, Ross N S, Sivalingam V. Implementation of green cooling/lubrication strategies in metal cutting industries: A state of the art towards sustainable future and challenges. *Sustain Mater Technol* **36**: e00641 (2023)
[4] Woydt M. The importance of tribology for reducing CO_2 emissions and for sustainability. *Wear* **474**: 203768 (2021)
[5] Tzanakis I, Hadfield M, Thomas B, Noya S M, Henshaw I, Austen S. Future perspectives on sustainable tribology. *Renew Sust Energ Rev* **16**(6): 4126–4140 (2012)
[6] Bondarev A, Al-Rjoub A, Yaqub T B, Polcar T, Fernandes F. TEM study of the oxidation resistance and diffusion processes in a multilayered TiSiN/TiN (Ag) coating designed for tribological applications. *Appl Surf Sci* **609**: 155319 (2022)
[7] Bondarev A V, Kiryukhantsev-Korneev P V, Sidorenko D A, Shtansky D V. A new insight into hard low friction MoCN–Ag coatings intended for applications in wide temperature range. *Mater Des* **93**: 63–72 (2016)
[8] Ju H B, Ding N, Xu J H, Yu L H, Geng Y X, Yi G, Wei T Y. Improvement of tribological properties of niobium nitride films via copper addition. *Vacuum* **158**: 1–5 (2018)
[9] Dai X, Wen M, Wang J, Cui X R, Wang X, Zhang K. The tribological performance at elevated temperatures of MoNbN–Ag coatings. *Appl Surf Sci* **509**: 145372 (2020)
[10] Popović M, Novaković M, Pjević D, Vaňa D, Jugović D, Tošić D, Noga P. Investigating on the microstructure and optical properties of Au, Ag and Cu implanted TiN thin films: The effects of surface oxidation and ion-induced defects. *J Alloys Compd* **976**: 173046 (2024)
[11] Ju H B, Kong F L, Xu J H, Geng Y X, Zhang C K, Luan J. Influence of Ag on the microstructure, mechanical and tribological properties of SiC–Ag composite film deposited by the industrial DC magnetron sputtering system. *Vacuum* **218**: 112672 (2023)
[12] Ju H B, Huang K H, Luan J, Geng Y X, Yang J F, Xu J H. Evaluation under temperature cycling of the tribological properties of Ag–SiN_x films for green tribological applications. *Ceram Int* **49**(18): 30115–30124 (2023)
[13] Wang W Z, Pu J B, Cai Z B, Zheng S X, Wei Y. Insights into friction properties and mechanism of self-lubricating MoVN–Ag films at high temperature. *Vacuum* **176**: 109332 (2020)
[14] Liu C K, Ju H B, Xu J H, Yu L H, Zhao Z T, Geng Y X, Zhao Y. Influence of copper on the compositions, microstructure and room and elevated temperature tribological properties of the molybdenum nitride film. *Surf Coat Tech* **395**: 125811 (2020)
[15] Chen Y J, Sun J F, Liu Y, Li Q, Xiao S, Su F H. Microstructure, mechanical and high-temperature tribological properties of MoS_2–Cr–Ag composite films. *Surf Coat Tech* **452**: 129135 (2023)
[16] Bian S N, Yu L H, Jia P, Xu J H. Study on microstructure, mechanical properties and corrosion resistance of NbCN–Cu composite films. *Int J Refract Met H* **107**: 105885 (2022)
[17] Zhang H, Zhang R, Zhao X Y, Li X D, Chen B T, Li Y H, Wang P. High-temperature tribological properties of the novel NiCr(MoNb)$_x$–Ag self-lubricating composite films. *Surf Coat Tech* **471**: 129916 (2023)
[18] Cao H T, Wen F, Kumar S, Rudolf P, De Hosson J T M, Pei Y T. On the S/W stoichiometry and triboperformance of $WS_xC(H)$ coatings deposited by magnetron sputtering. *Surf Coat Tech* **365**: 41–51 (2019)
[19] Dai M J, Wei C B, Zhou K S, Zhu M, Hou H J, Lin S S, Tong X. Properties of W/DLC/W–S–C composite films fabricated by magnetron sputtering. *T Nonferr Metal Soc* **25**: 3002–3011 (2015)
[20] Wu J H, Rigney D A, Falk M L, Sanders J H, Voevodin A A, Zabinski J S. Tribological behavior of WC/DLC/WS_2 nanocomposite coatings. *Surf Coat Tech* **188–189**: 605–611 (2004)
[21] Ju H B, Zhou R, Liu S J, Yu L H, Xu J H, Geng Y X. Enhancement of the tribological behavior of self-lubricating nanocomposite Mo_2N/Cu films by adding the amorphous SiN_x. *Surf Coat Tech* **423**: 127565 (2021)
[22] Zhang G J, Fan T X, Wang T, Chen H L. Microstructure, mechanical and tribological behavior of MoN_x/SiN_x multilayer coatings prepared by magnetron sputtering. *Appl Surf Sci* **274**: 231–236 (2013)
[23] Ju H B, Xu L Y, Luan J, Geng Y X, Xu J H, Yu L H, Yang J F, Fernandes F. Enhancement on the hardness and oxidation resistance property of TiN/Ag composite films for high temperature applications by addition of Si. *Vacuum* **209**: 111752 (2023)
[24] Hu J J, Muratore C, Voevodin A. Silver diffusion and high-temperature lubrication mechanisms of YSZ–Ag–Mo based nanocomposite coatings. *Compos Sci Technol* **67**: 336–347 (2007)
[25] Muratore C, Hu J J, Voevodin A A. Tribological coatings for lubrication over multiple thermal cycles. *Surf Coat Tech* **203**: 957–962 (2009)
[26] Ju H B, Zhou R, Luan J, Yu L H, Xu J H, Zuo B, Yang J F, Geng Y X, Zhao L J, Fernandes F. Multilayer Mo_2N–Ag/SiN_x films for demanding applications: Morphology, structure and temperature-cycling tribological properties. *Mater Des* **223**: 111128 (2022)
[27] Luan J, Kong F L, Xu J H, Fernandes F, Evaristo M, Dong S T, Cavaleiro A, Ju H B. Deciphering the mechanical strengthening mechanism: Soft metal doping in ceramic matrices—A case study of TiN–Ag films. *Mater Design* **248**: 113489 (2024)
[28] Köstenbauer H, Fontalvo G A, Keckes J, Mitterer C. Intrinsic stresses and stress relaxation in TiN/Ag multilayer coatings during thermal cycling. *Thin Solid Films* **516**(8): 1920–1924 (2008)
[29] Mejía H D, Echavarría A M, Bejarano G G. Influence of Ag–Cu

nanoparticles on the microstructural and bactericidal properties of TiAlN(Ag, Cu) coatings for medical applications deposited by direct current (DC) magnetron sputtering. *Thin Solid Films* **687**: 137460 (2019)

[30] Li H, Li J L, Kong J, Huang J W, Wu Q J, Xiong D S. Achieving high toughness and wear resistance for hard TaN–Ag films actuated by Ag. *Int J Refract Met H* **111**: 106076 (2023)

[31] Liu E Y, Zhang J H, Chen S, Du S M, Du H L, Cai H, Wang L L. High temperature negative wear behaviour of VN/Ag composites induced by expansive oxidation reaction. *Ceram Int* **47**(11): 15901–15909 (2021)

[32] Ren P, Zhang S Z, Qiu J X, Yang X Y, Wang W W, Li Y, Si Y X, Wang G G, Wen M. Self-lubricating behavior of VN coating catalyzed by solute Ag atom under dry friction and oil lubrication. *Surf Coat Tech* **409**: 126845 (2021)

[33] Ju H B, Ding N, Xu J H, Yu L H, Geng Y X, Ahmed F. The tribological behavior of niobium nitride and silver composite films at elevated testing temperatures. *Mater Chem Phys* **237**: 121840 (2019)

[34] Bandyopadhyay A, Traxel K D, Bose S. Nature-inspired materials and structures using 3D printing. *Mater Sci Eng R Rep* **145**: 100609 (2021)

[35] Liu Y, Zhu C L, Wan F Q, Fang W J, Xue B Y, Zheng Z Z, Ping H, Xie H, Wang H, Wang W M, et al. Biotemplating synthesis of organized structures inspired by biological processes. *Giant* **11**: 100108 (2022)

[36] Jiao D, Liu ZQ, Zhu YK, Weng ZY, Zhang ZF. Mechanical behavior of mother-of-pearl and pearl with flat and spherical laminations. *Mater Sci Eng C* **68**: 9–17 (2016)

[37] Ji H M, Li X W. Mechanical behavior of hierarchically structured nacre. In: *Comprehensive Structural Integrity*, 2nd edn. Aliabadi F M H, Soboyejo W, Eds. Oxford (UK): Elsevier, 2023: 161–184.

[38] Madhav, D. Buffel B, Moldenaers P, Desplentere F, Vandeginste V. A review of nacre-inspired materials: Chemistry, strengthening-deformation mechanism, synthesis, and applications. *Prog Mater Sci* **139**: 101168 (2023)

[39] Ju H B, Wang R, Wang W X, Xu J H, Yu L H, Luo H. The microstructure and tribological properties of molybdenum and silicon nitride composite films. *Surf Coat Tech* **401**: 126238 (2020)

[40] Zhang Q G, Zhou Y, Zhang G J, Zhang L C, Xie Z M, Zuo L, Ju H B, Fang Q F, Liu J G, Yang J F. Nanocomposite Mo–Ag–N lubricating, wear resistant and hard coatings fabricated by magnetron sputtering. *Mater Sci Eng B* **286**: 116066 (2022)

[41] Ju H B, Wang R, Ding N, Yu L H, Xu J H, Ahmed F, Zuo B, Geng Y X. Improvement on the oxidation resistance and tribological properties of molybdenum disulfide film by doping nitrogen. *Mater Des* **186**: 108300 (2020)

[42] Liu Q, Fang Q F, Liang F J, Wang J X, Yang J F, Li C. Synthesis and properties of nanocomposite MoSiN hard films. *Surf Coat Tech* **201** (3-4): 1894–1898 (2006)

[43] Ju H B, Xu J H. Influence of vanadium incorporation on the microstructure, mechanical and tribological properties of Nb–V–Si–N films deposited by reactive magnetron sputtering. *Mater Charact* **107**: 411–418 (2015)

[44] Wang R, Li J L, Wang Y X, Hu J M, Wu H Z. High temperature oxidation behavior and mechanical properties of TiAlN/SiN decorative films on borosilicate glass by magnetron sputtering. *Thin Solid Films* **584**: 72–77 (2015)

[45] Rismani E, Yeo R, Mirabolghasemi H, Kwek W M, Yang H, Bhatia C S. An ultrathin multilayer TiN/SiN wear resistant coating for advanced magnetic tape drive heads. *Thin Solid Films* **556**: 354–360 (2014)

[46] Chawla V, Jayaganthan R, Chandra R. Microstructural and mechanical properties of sputter deposited TiN/SiN_x multilayer thin films. *Mater Chem Phys* **122**(2–3): 424–430 (2010)

[47] Uglov V V, Kvasov N T, Remnev G E, Shymanski V I, Korenevski E L, Zlotski S V, Abadias G, O'Connel J, van Vuuren A. Size effect in AlN/SiN multilayered films irradiated with helium and argon ions. *Nucl Instrum Meth B* **435**: 228–235 (2018)

[48] Saladukhin I A, Abadias G, Uglov V V, Zlotski S V, Michel A, Janse van Vuuren A. Thermal stability and oxidation resistance of ZrSiN nanocomposite and ZrN/SiN_x multilayered coatings: A comparative study. *Surf Coat Tech* **332**: 428–439 (2017)

[49] Abadias G, Uglov V V, Saladukhin I A, Zlotski S V, Tolmachova G, Dub S N, van Vuuren A J. Growth, structural and mechanical properties of magnetron-sputtered ZrN/SiN_x nanolaminated coatings. *Surf Coat Tech* **308**: 158–167 (2016)

[50] Hovsepian P E, Lewis D B, Münz W D. Recent progress in large scale manufacturing of multilayer/superlattice hard coatings. *Surf Coat Tech* **133–134**: 166–175 (2000)

[51] Zhang S, Li J H, Tu R, Ando K, Gao T H. Improved hardness of semi-coherent TiN/CrN nano-multilayer coating through manipulation of structure evolution. *Mater Sci Eng A* **886**: 145728 (2023)

[52] Liang B H, Hsieu F S, Wu F B. Modulation effect on mechanical properties of nanolayered MoN/MoSiN coatings. *Surf Coat Tech* **436**: 128278 (2022)

[53] Liu Y M, Wang M R, Liu L S, Song H Z, Hu T W, Xiong J J, Zhai Z F, Zhao X, Zhang C Y, Yang B, et al. Effect of the interfacial microstructure on hardness of multi-layer diamond coatings. *Surf Coat Tech* **464**: 129541 (2023)

[54] Lin B, Li J J, Wang Z J, Wang J C. Dislocation nucleation from Zr–Nb bimetal interfaces cooperating with the dynamic evolution of interfacial dislocations. *Int J Plast* **135**: 102830 (2020)

[55] Zeng Y, Hunter A, Beyerlein I J, Koslowski M. A phase field dislocation dynamics model for a bicrystal interface system: An investigation into dislocation slip transmission across cube-on-cube interfaces. *Int J Plast* **79**: 293–313 (2016)

[56] Wei M Z, Shi J, Ma Y J, Cao Z H, Meng X K. The ultra-high enhancement of hardness and elastic modulus in Ag/Nb multilayers. *Mater Sci Eng A* **651**: 155–159 (2016)

[57] Zhen Y, Chen M H, Yu C T, Yang Z B, Qi Y, Wang F H. High temperature self-lubricating Ti–Mo–Ag composites with exceptional high mechanical strength and wear resistance. *J Mater Sci Technol* **180**: 80–90 (2024)

[58] Tan H, Sun Q C, Zhu S Y, Cheng J, Wang S, Yang J. High temperature tribological behavior of Mo–12Si–8.5B alloy reinforced with MoAlB ceramic. *Tribol Int* **150**: 106344 (2020)

[59] Wenda E. High temperature reactions in the MoO_3–Ag_2O system. *J Therm Anal Calorim* **53**(3): 861–870 (1998)

[60] Singh A K, Atheaya D, Tyagi R, Ranjan V. Friction and wear behavior of atmospheric plasma sprayed NiMoAl–Ag–hBN coatings at elevated temperatures. *Surf Coat Tech* **466**: 129650 (2023)

[61] Ben Khemis S, Burov E, Montigaud H, Skrelic D, Gouillart E, Cormier L. Structural analysis of sputtered amorphous silica thin films: A Raman spectroscopy investigation. *Thin Solid Films* **733**: 138811 (2021)

[62] Geng D S, Li H Q, Chen Z L, Xu Y X, Wang Q M. Microstructure, oxidation behavior and tribological properties of AlCrN/Cu coatings deposited by a hybrid PVD technique. *J Mater Sci Technol* **100**: 150–160 (2022)

[63] Ju H B, Athmani M, Luan J, AL-Rjoub A, Cavaleiro A, Yaqub T B, Chala A, Ferreira F, Fernandes F. Insights into the oxidation resistance mechanism and tribological behaviors of multilayered TiSiN/CrV_xN hard coatings. *Int J Miner Metall Mater* **30**(12): 2459–2468 (2023)

[64] Magnifouet G, Vallet M, Meslin E, Walls M, Bouillet C, Arabski J, Pierron-Bohnes V. Strains in Fe/Cr/Fe trilayers and $(Fe/Cr)_5$/Fe multilayers epitaxied on MgO and MgO/$SrTiO_3$. *Thin Solid Films* **780**: 139949 (2023)

[65] Lu C, Fu Y Y, Jia J H, Yi G W, Xie E Q, Guo H J. Effect of substrate temperatures on the properties of PLD Mo–V–Ag–O nanocomposite thin films. *Vacuum* **167**: 357–363 (2019)

[66] Khan M K, Tahir S A, Ashfaq A, Ali A, Ahmad W, Haneef M, Mushtaq S, Saeed R, Khan K M, Shabbir K. Enhancement of the structural, optical and thermoelectric properties of thermally

evaporated $AgMoO_3$ thin film by post-annealing. *Opt Mater* **128**: 112406 (2022)
[67] Lv Y J, Sun H L, Lian X X, Zhang H G, Shi P Y, Ma F, Wang G X. Surface morphology evolution behavior and SERS performance of Mo–Ag–Cu–Co films. *Appl Surf Sci* **604**: 154594 (2022)
[68] Hao E K, An Y L, Chen J, Zhao X Q, Hou G L, Chen J M, Gao M Z, Yan F Y. *In-situ* formation of layer-like Ag_2MoO_4 induced by high-temperature oxidation and its effect on the self-lubricating properties of NiCoCrAlYTa/Ag/Mo coatings. *J Mater Sci Technol* **75**: 164–173 (2021)
[69] Zhang M D, Zhou F, Fu Y Q, Wang Q Z, Zhou Z F. Influence of Ag target current on the structure and tribological properties of CrMoSiCN/Ag coatings in air and water. *Tribol Int* **160**: 107059 (2021)
[70] Yang J J, Jia J H, Li X, Lu C, Feng X C. Synergistic lubrication of Ag and Ag_2MoO_4 nanoparticles anchored in plasma-sprayed YSZ coatings: Remarkably-durable lubricating performance at 800 °C. *Tribol Int* **153**: 106670 (2021)
[71] Gautam R K S, Rao U S, Tyagi R. High temperature tribological properties of Ni-based self-lubricating coatings deposited by atmospheric plasma spray. *Surf Coat Tech* **372**: 390–398 (2019)

Hongbo Ju is a full professor at Jiangsu University of Science and Technology and Marie-Curie-Research-Fellow from Marie Skłodowska-Curie actions (MSCA) with a number of MSCA-COFUND-5100-237/2023-9. His research interests include thin solid coatings (PVDs), superhard nitride coatings, oxidation resistance, and self-lubrication and wear resistance coatings suitable for high-temperature applications. He published more than 100 papers in international peer review journals.

Jing Luan is a Ph.D. candidate at the University of Coimbra and is a member of Centre for Mechanical Engineering, Materials and Processes (CEMMPRE). Her research pursuits encompass various facets, notably thin solid coatings (PVDs), superhard nitride coatings, oxidation resistance, self-lubrication, and wear resistance coatings tailored for high-temperature applications.